nature electronics

ARTICLES

https://doi.org/10.1038/s41928-022-00744-8

Tilted spin current generated by the collinear antiferromagnet ruthenium dioxide

Arnab Bose[1,2,7], Nathaniel J. Schreiber[3,7], Rakshit Jain[1,2,7], Ding-Fu Shao[4], Hari P. Nair[3], Jiaxin Sun[3], Xiyue S. Zhang[1], David A. Muller[1,5], Evgeny Y. Tsymbal[4], Darrell G. Schlom[3,5,6] and Daniel C. Ralph[2,5]✉

Symmetry plays a central role in determining the polarization of spin currents induced by electric fields. It also influences how these spin currents generate spin-transfer torques in magnetic devices. Here we show that an out-of-plane damping-like torque can be generated in ruthenium dioxide (RuO_2)/permalloy devices when the Néel vector of the collinear antiferromagnet RuO_2 is canted relative to the sample plane. By measuring characteristic changes in all three components of the electric-field-induced torque vector as a function of the angle of the electric field relative to the crystal axes, we find that the RuO_2 generates a spin current with a well-defined tilted spin orientation that is approximately parallel to the Néel vector. A maximum out-of-plane damping-like spin torque efficiency per unit electric field of $7 \pm 1 \times 10^3\ \Omega^{-1}\,m^{-1}$ is measured at room temperature. The observed angular dependence indicates that this is an antiferromagnetic spin Hall effect with symmetries that are distinct from other mechanisms of spin-current generation reported in antiferromagnetic and ferromagnetic materials.

For magnetic heterostructures in which an in-plane electric field causes a spin-current-generating layer to exert a spin-transfer torque on an adjacent magnetic layer, rotational and reflection symmetries present in the spin-current-generating layers typically restrict the allowed spin polarization of the electric-field-induced spin current to a single axis, in the sample plane and perpendicular to the applied electric field (**E**). This is unfortunate, because this spin orientation cannot drive efficient anti-damping switching of magnetic devices with perpendicular magnetic anisotropy. One way to avoid this problem is to lower the symmetry of the spin-current-generating material, which makes more general spin orientations possible. This has been demonstrated in materials in which the symmetry is lowered via the crystal structure[1–4] or ferromagnetic moments[5–14]. However, the resulting out-of-plane anti-damping torques have not been shown to be strong enough for practical applications. Alternatively, spin currents with out-of-plane spin components emerging from antiferromagnets have been predicted and measured[15–22]. This is potentially valuable because the spin-current generation in antiferromagnets appears to result primarily from mechanisms—exchange interactions and Berry curvature induced by non-collinear spin order—that could be stronger than the spin–orbit interactions (SOIs) that have been the previous focus of the field.

It was recently proposed that the collinear antiferromagnet ruthenium dioxide (RuO_2) might produce strong electric-field-induced spin currents with spin orientation approximately aligned along the Néel vector[23]. This spin generation has been identified[24] as the property of a general class of collinear antiferromagnets exhibiting momentum-dependent spin splitting[25,26]. In this mechanism, a spin-split band-structure, caused by inequivalent crystal environments for the two spin sublattices, yields spin currents with spin polarization parallel to the Néel vector. When the Néel vector is appropriately canted, the result can be a vertically flowing spin current with a strong out-of-plane spin component.

In this Article we report measurements of **E**-induced torques within RuO_2/permalloy (Py) devices. The full three-dimensional spin-orientation of the **E**-induced spin is extracted by measuring the **E**-induced torques as a function of the angles of both the applied magnetic field and the **E** relative to the crystal axes. We determine that RuO_2 produces an **E**-induced spin-current polarization aligned approximately (but not exactly) with the Néel vector $\mathcal{N}$, which is in good agreement with the spin-splitter mechanism for RuO_2. This mechanism is distinct from the recently reported spin Hall effect (SHE) in the collinear antiferromagnet Mn_2Au (ref. [21]). In Mn_2Au, the spin polarization of the spin current is perpendicular to $\mathcal{N}$, and the out-of-plane anti-damping torque is maximized when **E** is parallel to $\mathcal{N}$. In the spin-splitter mechanism in RuO_2, the spin polarization of the spin current is approximately parallel to $\mathcal{N}$, and the out-of-plane spin current requires $\mathcal{N}$ to be canted out of the sample plane.

SHE in RuO_2

RuO_2 is a conductive rutile oxide belonging to space group $P\frac{4_2}{m}nm$ (no. 136), with a globally centrosymmetric crystal structure (Fig. 1a). The crystal structure is the same as that of IrO_2, the SHE of which has been measured recently[27], although the two materials differ in that RuO_2 is an antiferromagnet while IrO_2 is non-magnetic. The band-structures of both materials contain Dirac nodal lines protected by non-symmorphic symmetries[28,29], which have the potential to generate strong SHEs. Recently, RuO_2 has also drawn considerable attention with the discovery of strain-stabilized superconductivity[30,31], anomalous antiferromagnetism[32,33], a crystal Hall effect[34,35] and predictions of a magnetic SHE[23] and giant tunnelling magnetoresistance[36,37].

[1]School of Applied and Engineering Physics, Cornell University, Ithaca, NY, USA. [2]Department of Physics, Cornell University, Ithaca, NY, USA. [3]Department of Materials Science and Engineering, Cornell University, Ithaca, NY, USA. [4]Department of Physics and Astronomy & Nebraska Center for Materials and Nanoscience, University of Nebraska, Lincoln, NE, USA. [5]Kavli Institute at Cornell for NanoScale Science, Ithaca, NY, USA. [6]Leibniz-Institut für Kristallzüchtung, Berlin, Germany. [7]These authors contributed equally: Arnab Bose, Nathaniel J. Schreiber, Rakshit Jain. ✉e-mail: dcr14@cornell.edu

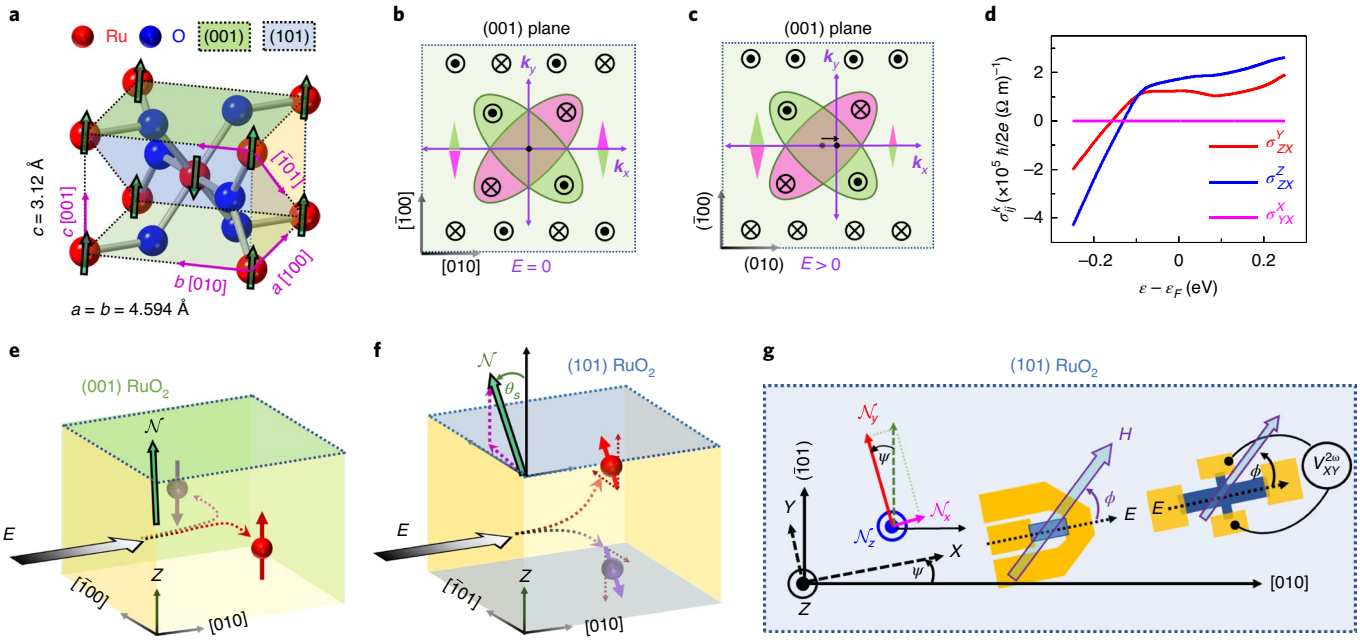

Fig. 1 | Time-reversal-odd spin Hall conductivity in RuO_2. **a**, The crystal structure of RuO_2 with spin orientations indicated (green arrows). **b**,**c**, Schematic diagrams of the spin-split Fermi surface of RuO_2 for up-spin and down-spin electrons with zero (**b**) and non-zero (**c**) electric field E applied in the [010] direction. The green and pink triangles denote the transverse flow of up- and down-spin electrons. **d**, Calculated time-odd spin Hall conductivity for a (101)-oriented RuO_2 film with applied electric field in the [010] direction, as a function of electron energy ε measured relative to the Fermi energy ε_F. **e**,**f**, Illustration of spin current generation due to the antiferromagnetic SHE for a (001)-oriented RuO_2 film (**e**) and a (101)-oriented film (**f**). $\mathcal{N}$ is the Néel vector and θ_S is the angle by which $\mathcal{N}$ is tilted from the out-of-plane direction. **g**, Sample schematics and definition of the coordinate axes for the (101)-oriented sample. The X direction is parallel to the applied electric field and ψ is the angle of the electric field relative to the [010] crystal axis. ϕ is the angle of the applied magnetic field H relative to the applied electric field. $V^{2\omega}_{XY}$ is the second-harmonic Hall voltage.

Within the structure of RuO_2 (Fig. 1a), the Ru atoms at the centre and corners of the unit cell have opposite spins, forming a collinear antiferromagnetic (AF) ordering with the Néel vector $\mathcal{N}$ oriented along the [001] or [00$\bar{1}$] axis (with perhaps a small canting)[32,33]. The centre and corner Ru atoms experience different oxygen environments, which leads to spin-split bands, as shown schematically in Fig. 1b[23]. As a result of this spin-split band-structure, theory predicts that, when an electric field **E** is applied, it can generate a spin current through an AF-SHE, even in the absence of any spin–orbit interaction (SOI). An example is shown in Fig. 1c, in which electric field **E** applied along the $\hat{X}$ axis ([010] direction) produces a spin current flowing along $\hat{Y}$ ([$\bar{1}$00] direction) with spin polarization along $\hat{Z}$ ([001] direction). This result is qualitatively similar to the conventional SHE in heavy metals, which is even under time reversal ($\mathcal{T}$-even). However, the origin of the AF-SHE is fundamentally different because it does not require SOI and it is odd under time reversal ($\mathcal{T}$-odd). If the crystal axes are rotated differently relative to the sample plane, the spin current can be calculated by an appropriate rotation of a spin Hall conductivity (SHC) tensor (Supplementary Section 4). In general, the flow of the spin current from this AF-SHE in RuO_2 will have a spin orientation $\hat{s}$ pointing approximately along $\mathcal{N}$, regardless of the electric field and spin-flow directions. RuO_2 possesses spin–orbit coupling, so it can also generate a $\mathcal{T}$-even spin–orbit torque. Our density functional theory calculation results (shown in Fig. 1d) predict that, in a single-domain RuO_2 antiferromagnet, the $\mathcal{T}$-odd SHC should be almost an order of magnitude larger than the $\mathcal{T}$-even SHC, given the SOI of RuO_2, and the spin orientation produced by the $\mathcal{T}$-even mechanism is not determined by $\mathcal{N}$ (Supplementary Section 4). These results are consistent with the prediction of ref. [23]. A $\mathcal{T}$-odd transverse spin current in magnetic systems is generally referred to as a magnetic SHE[15,18,38].

Based on the geometry of the $\mathcal{T}$-odd AF-SHE predicted for RuO_2, we expect very different symmetries for the **E**-induced torques depending on whether the Néel vector is oriented out of plane or canted partially into the sample plane. For (001)-oriented RuO_2 films, $\mathcal{N}$ and hence the **E**-generated spin orientation $\hat{s}$ should point approximately perpendicular to the sample plane (Fig. 1e). Because the flow of spin current generated by the AF-SHE in RuO_2 must be perpendicular to the [001] direction, the $\mathcal{T}$-odd AF-SHE mechanism should not generate any spin current flowing vertically toward the Py layer, and hence should not produce any spin-transfer torque related to the Néel vector in the (001)-oriented case. Therefore, for this geometry, the dominant **E**-induced torque should be the conventional torque generated by SOI, driven by a spin polarization oriented in-plane and perpendicular to **E**, that is, in the Y direction, or [$\bar{1}$00] for Fig. 1e. This can lead to both an in-plane damping-like (DL) torque with the symmetry $\tau^Y_{DL} = -\tau^Y_{DL,0}(\hat{m} \times \hat{Y} \times \hat{m})$ and/or an out-of-plane field-like (FL) torque $\tau^Y_{FL} = -\tau^Y_{FL,0}(\hat{m} \times \hat{Y})$. (We define signs as in ref. [39]. With these choices of sign, a positive $\tau^Y_{DL,0}$ corresponds to the sign of the SHE for Pt, and $\tau^Y_{FL,0}$ is positive for the Oersted field. All torques quoted are per unit magnetic moment with sign $\tau \propto d\hat{m}/dt$.)

For a (101)-oriented RuO_2 film, on the other hand, the [001] axis is canted away from the out-of-plane direction with components along both the out-of-plane [101]* and in-plane [$\bar{1}$01] directions (Fig. 1f). The consequence of the AF-SHE spin-splitter mechanism in this case can be understood simply by visualizing the diagram in Fig. 1e rotated about the [010] axis. The flow of the spin current is still perpendicular to the [001] axis and the spin polarization $\hat{s}$ remains parallel to the [001] axis, but now, because of the canting

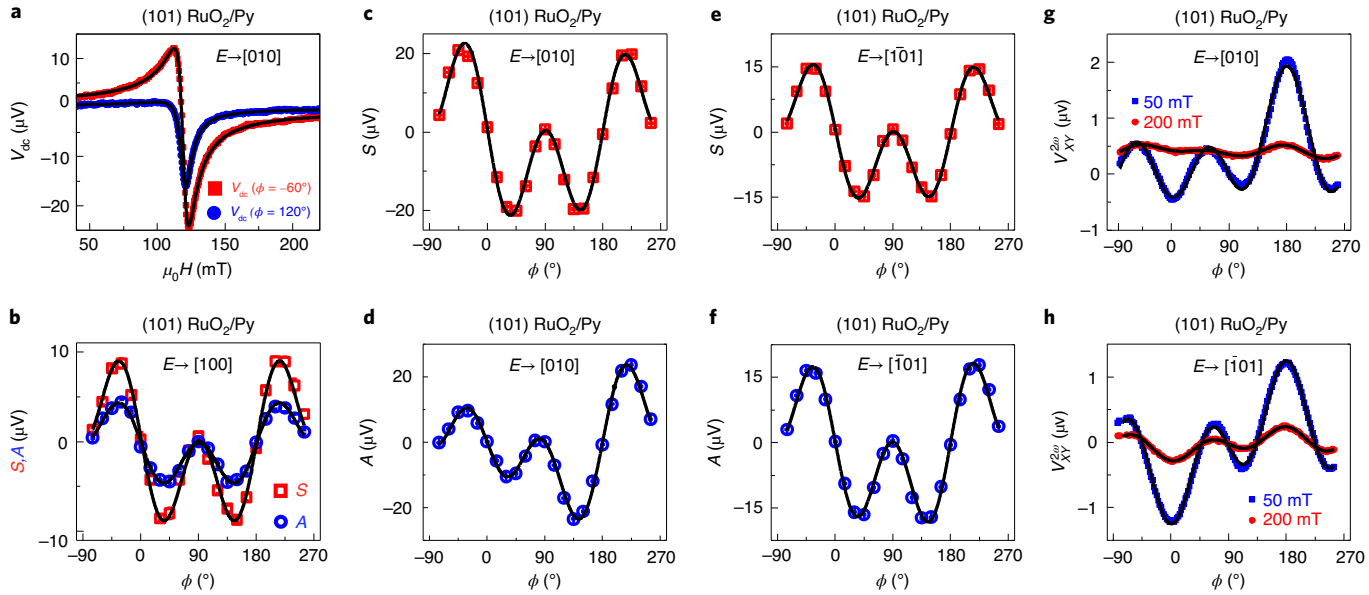

Fig. 2 | Spin-torque ferromagnetic resonance and second-harmonic Hall measurements. a, ST-FMR signals as a function of applied magnetic field measured for a (101)-oriented RuO_2(6 nm)/Py(4 nm) sample with electric field applied along the [010] axis with a 15 dBm, 10 GHz microwave drive at room temperature, along with fits to the sum of symmetric and antisymmetric line shapes. The two curves shown correspond to magnetic-field sweeps along the $\phi = -60°$ and $\phi = 120°$ directions. **b**, Symmetric resonance amplitude (S) versus in-plane magnetic-field angle (ϕ) (red squares) and antisymmetric resonance amplitude (A) versus ϕ (blue circles) for a (001)RuO_2(6 nm)/Py(4 nm) sample with electric field applied along the [100] axis. **c**,**d**, S versus ϕ (**c**) and A versus ϕ (**d**) for a (101)RuO_2(6 nm)/Py(4 nm) sample with electric field applied along the [010] axis ($\psi = 0°$). **e**,**f**, S versus ϕ (**e**) and A versus ϕ (**f**) for a (101)RuO_2(6 nm)/Py(4 nm) sample with electric field applied along the [$\bar{1}$01] axis ($\psi = 90°$). **g**,**h**, Second-harmonic Hall signals ($V_{XY}^{2\omega}$) for a (101) RuO_2(6 nm)/Py(4 nm) sample with electric field applied along the [010] direction (**g**) and the [$\bar{1}$01] direction (**h**) for two different magnitudes of in-plane magnetic field.

of the [001] axis, both the spin polarization and flow have components both perpendicular to the sample plane and in the sample plane. This geometry therefore allows the AF-SHE in RuO_2 to be distinguished clearly from the conventional SHE in non-magnetic materials. If we define the X direction as parallel to the applied electric field **E** and the Z direction as out of plane, then, depending on the orientation of **E** relative to the crystal axes, the AF-SHE can produce SHC with non-zero components σ_{ZX}^{Y} (generating, for example, in-plane damping-like torque), σ_{ZX}^{X} (generating, for example, $\tau_{DL}^{X} = \tau_{DL,0}^{X}(\hat{m} \times \hat{X} \times \hat{m})$) and σ_{ZX}^{Z} (generating, for example, $\tau_{DL}^{Z} = \tau_{DL,0}^{Z}(\hat{m} \times \hat{Z} \times \hat{m})$). A symmetry analysis of the SHC tensor (Supplementary Section 4) predicts that the components of damping-like torque generated by the AF-SHE will follow a signature angular-dependence pattern. In a (101)-oriented RuO_2 film, if the **E**-generated spin $\hat{s}$ is oriented at an angle θ_s tilted away from the out-of-plane (Z=[101]*) axis towards the [$\bar{1}$01] direction and $\hat{E}$ is applied at an angle ψ with respect to the in-plane [010] axis, the components of damping-like torque efficiencies per unit electric field generated by the AF-SHE should follow

$$\xi_{DL,E}^{Y} \equiv \frac{2e}{\hbar}\frac{\mu_0 M_S t_{FM}}{\gamma}\frac{\tau_{DL,0}^{Y}}{E} = C_1 \sin^2\theta_s \cos^2\psi + C_0, \quad (1)$$

$$\xi_{DL,E}^{Z} \equiv \frac{2e}{\hbar}\frac{\mu_0 M_S t_{FM}}{\gamma}\frac{\tau_{DL,0}^{Z}}{E} = C_1 \cos\theta_s \sin\theta_s \cos\psi, \quad (2)$$

$$\xi_{DL,E}^{X} \equiv \frac{2e}{\hbar}\frac{\mu_0 M_S t_{FM}}{\gamma}\frac{\tau_{DL,0}^{X}}{E} = C_1 \sin^2\theta_s \cos\psi \sin\psi, \quad (3)$$

where C_0 and C_1 are constants, M_S is the saturation magnetization, t_{FM} is the thickness of the ferromagnetic layer and γ is the gyromagnetic ratio. (The C_0 term can be generated by conventional SHE, independent of AF-SHE.)

In micrometre-scale devices of the sort we study, we expect to have many AF domains, with nearly equal numbers having $\mathcal{N}$ pointing along [001] and [00$\bar{1}$]. If the fractions of the two domain variants are exactly equal, this should lead to zero $\mathcal{T}$-odd spin current. Nonetheless, in a multi-domain scenario, we can still obtain either a non-zero $\mathcal{T}$-odd SHC due to imperfect cancellation between domains or a non-zero $\mathcal{T}$-even SHC due to non-zero SOI. We will refer to a non-trivial spin Hall torque with a well-defined spin orientation $\hat{s}$ (and therefore following the signature angular dependence in equations (1) to (3)) as an AF-SHE for either the $\mathcal{T}$-odd or $\mathcal{T}$-even mechanism.

Techniques for extracting E-induced torque vectors

To investigate the SHC of RuO_2, we measure the **E**-induced torques acting on an in-plane-magnetized $Ni_{80}Fe_{20}$ (Py) layer (4 nm) deposited by sputtering on top of epitaxial RuO_2 thin films (3–9 nm). We analyse films grown on both (001)- and (101)-oriented TiO_2 substrates to study two different orientations of the Néel vector relative to the sample plane. Details of sample preparation are provided in Methods and Supplementary Section 1.

We measure the **E**-generated torques in Py/RuO_2 bilayers using angle-dependent spin-torque ferromagnetic resonance (ST-FMR)[1,40,41], and we verify the results using the in-plane-anisotropy harmonic Hall (HH)[42] technique. For ST-FMR measurements, the Py/RuO_2 bilayer is patterned into a wire with microwave-compatible contacts, as shown in Fig. 1g. On each sample chip we make several such devices oriented at different angles relative to the crystal axes to vary the angle ψ of **E** relative to the [010] direction. We apply a fixed-frequency microwave current and sweep an in-plane magnetic field at an angle ϕ with respect to the current flow direction (Fig. 1g), repeating the measurement for each

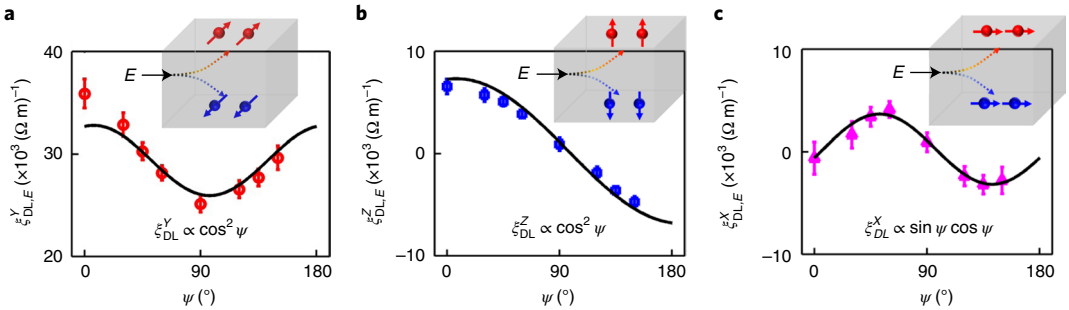

Fig. 3 | Determination of the vector components of the damping-like torque. a–c, For (101)RuO_2(6 nm)/Py(4 nm) samples, the dependence of the measured components of the damping-like torque efficiency per unit applied electric field (E) on the angle (ψ) of the electric field relative to the [010] direction, corresponding to the $\hat{Y}$ component of the spin current (**a**), the $\hat{Z}$ component (**b**) and the $\hat{X}$ component (**c**) as defined in Fig. 1g. Error bars are standard deviations due primarily to uncertainties in the fits of the ST-FMR amplitudes versus the magnetic field angle.

sample for field angles from $\phi = -90°$ to 270° in steps of 15°. Torques acting on the magnet from the microwave current induce magnetic precession and corresponding resistance oscillations due to the bilayer's anisotropic magnetoresistance. Mixing between the resistance oscillations and the oscillating current results in d.c. voltage signals near resonance, the magnetic-field dependence of which can be fit to the sum of the symmetric and antisymmetric Lorentzian peak shapes[1,40,41] $V_S = S\left(\frac{\Delta^2}{(H-H_0)^2+\Delta^2}\right)$ and $V_A = A\left(\frac{(H-H_0)\Delta}{(H-H_0)^2+\Delta^2}\right)$ (Fig. 2a). Amplitudes S and A are related to the in-plane and out-of-plane **E**-induced torques, Δ is the linewidth and H_0 is the resonant field. In the most general case when the spin polarization that generates the **E**-induced torque has components along all of the X, Y and Z axes, the allowed angular dependences for the coefficients S and A are[1,40,41]

$$S = S^Y_{DL}\cos\phi\ \sin 2\phi + S^X_{DL}\sin\phi\ \sin 2\phi + S^Z_{FL}\sin 2\phi, \quad (4)$$

$$A = A^Y_{FL}\cos\phi\ \sin 2\phi + A^X_{FL}\sin\phi\ \sin 2\phi + A^Z_{DL}\sin 2\phi, \quad (5)$$

where S^Y_{DL}, S^X_{DL} and A^Z_{DL} are coefficients for the damping-like torque generated by the SHCs, σ^Y_{ZX}, σ^X_{ZX} and σ^Z_{ZX} respectively, and A^Y_{FL}, A^X_{FL} and S^Z_{FL} are their field-like-torque counterparts (and A^Y_{FL} also contains the contribution from the Oersted torque). In our samples we can tell that the Oersted field is the dominant source for A^Y_{FL} because there is good agreement between the measured strength of the out-of-plane field-like torque and the estimated contribution from the Oersted field due to the current flow through the RuO_2 layer (Supplementary Sections 2 and 3). In this case, we can use the value of A^Y_{FL} as a measure of the current density in the RuO_2, which allows us to quantify the amplitude of the damping-like torque efficiencies per unit current density in the RuO_2 (j) as[40]

$$\xi^X_{DL,j} = \frac{S^X_{DL}}{A^Y_{FL}}\frac{e\mu_0 M_S t_{HM} t_{FM}}{\hbar}\sqrt{1+\left(\frac{M_{eff}}{H_0}\right)}, \quad (6)$$

$$\xi^Y_{DL,j} = \frac{S^Y_{DL}}{A^Y_{FL}}\frac{e\mu_0 M_S t_{HM} t_{FM}}{\hbar}\sqrt{1+\left(\frac{M_{eff}}{H_0}\right)}, \quad (7)$$

$$\xi^Z_{DL,j} = \frac{A^Z_{DL}}{A^Y_{FL}}\frac{e\mu_0 M_S t_{HM} t_{FM}}{\hbar}. \quad (8)$$

Here, $\mu_0 M_{eff}$ is the magnetic anisotropy (0.86 ± 0.03 T for the (101) devices and 0.68 ± 0.04 T for the (001) devices) measured by performing ST-FMR for a sequence of microwave frequencies and fitting the resonance fields to the Kittel equation. The saturation magnetization is $\mu_0 M_S = 0.87 \pm 0.02$ T, as measured by vibrating sample magnetometry, and t_{HM} and t_{FM} are the thicknesses of the RuO_2 and Py, respectively. The damping-like torque efficiencies per unit applied electric field ($\xi^k_{DL,E}$) for each component of torque k can be obtained by dividing by the resistivity ρ_{xx} of the RuO_2 film:

$$\xi^k_{DL,E} = \xi^k_{DL,j}/\rho_{xx}. \quad (9)$$

For 6-nm-thick RuO_2 at room temperature, ρ_{xx} is ~140 μΩ cm for (101)-oriented films and 275 μΩ cm for (001) films (compared to 70 μΩ cm for the 4-nm-thick Py). The components of the torque efficiencies per unit applied electric field $\xi^k_{DL,E}$ should be equal to the corresponding components of the SHC tensor $\sigma^k_{ZX}/[\hbar/(2e)]$ times an interfacial spin transparency that is less than or equal to 1.

For the in-plane HH method, we apply a low-frequency alternating current (1,327 Hz) and measure both the first- and second-harmonic Hall voltages as a function of the angle of rotation ϕ of an in-plane magnetic field (Fig. 1g). The a.c. current generates alternating torques that result in oscillations in the Hall resistance due to the planar Hall effect and anomalous Hall effect. Mixing between the oscillating Hall resistance and the a.c. current results in a second-harmonic signal that can be expressed as[2,42,43]

$$V^{2\omega}_{XY} = D^Y_{DL}\cos\phi + D^X_{DL}\sin\phi + D^Z_{DL}\cos 2\phi + F^Y_{FL}\cos\phi\cos 2\phi + F^X_{FL}\sin\phi\cos 2\phi + F^Z_{FL}. \quad (10)$$

Damping-like torques generated by the X, Y and Z components give rise to D^X_{DL}, D^Y_{DL} and D^Z_{DL}, respectively, and the field-like torque counterparts give rise to F^X_{FL}, F^Y_{FL} and F^Z_{FL}. The contributions from **E**-induced torques are distinguished from thermoelectric voltages based on their dependence on the magnetic-field magnitude. Supplementary Section 2 provides details of how the SHCs are calculated based on the HH measurements.

E-induced torques for different crystal orientations of RuO_2

Figure 2b shows the ϕ dependence of the ST-FMR amplitudes S (red squares) and A (blue circles) for a (001)-oriented RuO_2(6 nm)/Py(4 nm) sample when **E** is applied along the [100] axis. This is the crystal orientation for which $\mathcal{N}$ is oriented out of plane so that the AF-SHE should produce no unconventional **E**-induced torque on the Py layer by either the $\mathcal{T}$-odd or $\mathcal{T}$-even mechanism. We find that this is indeed the case. Both the symmetric component S and the antisym-

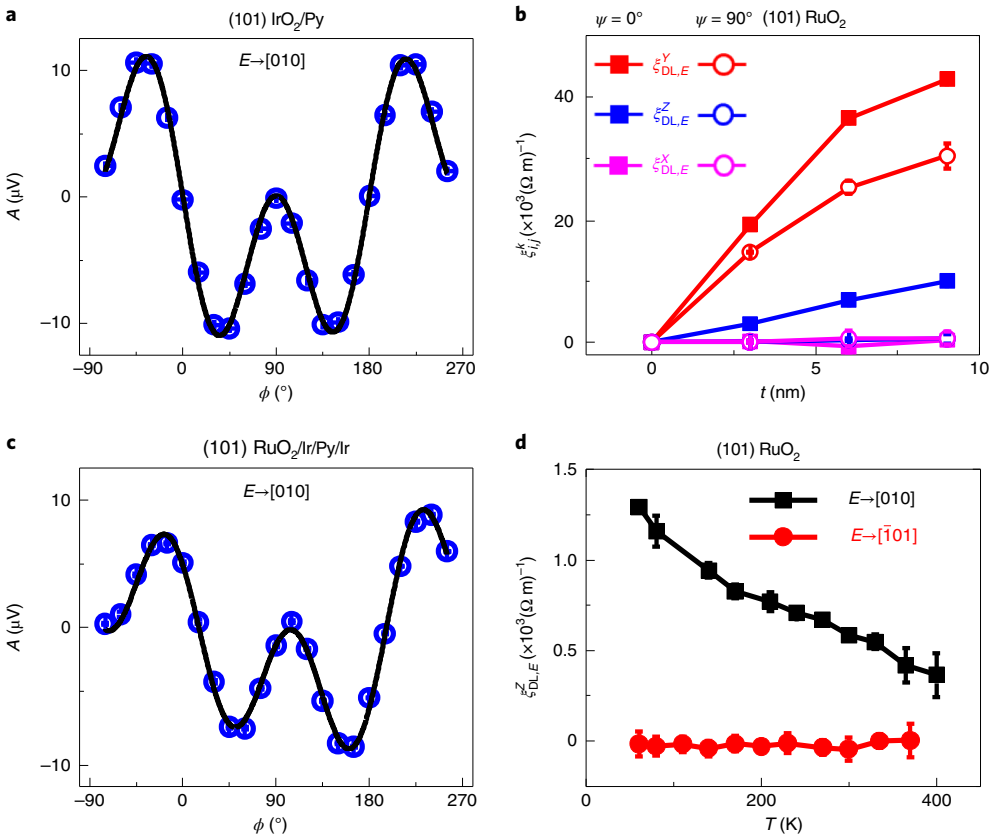

Fig. 4 | Comparison of RuO_2 and IrO_2 and the dependence of the torque from RuO_2 on layer thickness and temperature. a, Antisymmetric ST-FMR component *A* versus ϕ for a (101)IrO_2(6 nm)/Py(4 nm) sample with electric field (*E*) applied along the [010] direction ($\psi = 0°$), showing the absence of any unconventional torques from non-magnetic (101)IrO_2. **b**, Measured damping-like spin torque efficiencies per unit applied electric field in (101)RuO_2/Py(4 nm) samples as a function of RuO_2 thickness for $\psi = 0°$ (filled squares) and $\psi = 90°$ (open circles). **c**, *A* versus ϕ for a (101)RuO_2(9 nm)/Ir(1 nm)/Py(4 nm)/Ir(1 nm) sample with electric field applied along the [010] direction ($\psi = 0°$), showing the persistence of unconventional torques even with an Ir spacer layer. **d**, Out-of-plane damping-like spin-torque efficiency per unit electric field for a (101)RuO_2(6 nm)/Py(4 nm) sample as a function of temperature for $\psi = 0°$ (black squares) and $\psi = 90°$ (red circles). Error bars in **b** and **d** are standard deviations due primarily to uncertainties in the fits of the ST-FMR amplitudes versus magnetic field angle.

metric component *A* can be fitted well simply using the conventional torque terms $\propto \cos\phi \sin 2\phi$ that occur in ordinary heavy metals[40]. The strength of the symmetric term corresponds to a spin torque efficiency per unit electric field of $\xi^Y_{DL,E} = (1.8 \pm 0.4) \times 10^4\ (\Omega\,m)^{-1}$, as determined from equation (7).

The ST-FMR results for a (101)-oriented RuO_2(6 nm)/Py(4 nm) sample, the geometry for which $\mathcal{N}$ is tilted away from the out-of-plane direction, are shown in Fig. 2c–h. The data for **E** in the [010] direction ($\psi = 0°$ within alignment accuracy) are presented in Fig. 2c,d. The symmetric component of the ST-FMR signal has an angular dependence similar to the (001) sample; only the conventional damping-like SHE term $S^Y_{DL} \cos\phi \sin 2\phi$ is required to fit the results (Fig. 2c), and the corresponding torque efficiency is $\xi^Y_{DL,E} = (3.6 \pm 0.6) \times 10^4\ (\Omega\,m)^{-1}$ (or $\xi^y_{DL,j} = 0.049 \pm 0.008$). Note, however, that the antisymmetric component is very different than for the (001)-oriented film. For the (101)-oriented case, *A* cannot be fit only by the $A^Y_{FL} \cos\phi \sin 2\phi$ term; there is also a significant $A^Z_{DL} \sin 2\phi$ contribution corresponding to an out-of-plane damping-like torque (with $\xi^Z_{DL,E} = (7 \pm 1) \times 10^3\ (\Omega\,m)^{-1}$). This additional term is also consistent with our HH measurements (Fig. 2g) as $V^{2\omega}_{XY}$ requires the term $D^Z_{DL} \cos 2\phi$ for the fitting in addition to the conventional fitting function[2] $D^Y_{DL} \cos\phi + F^Y_{FL} \cos\phi \cos 2\phi$ (Supplementary Section 2). In contrast, when **E** is applied along the [$\bar{1}$01] axis ($\psi = 90°$) for the (101)-oriented case, we observe only conventional spin torques, that is, $\xi^Y_{DL,E} \neq 0$, $\xi^X_{DL,E} \approx 0$, $\xi^Z_{DL,E} \approx 0$, as both the *S* and *A* amplitudes in ST-FMR can be fit by $\cos\phi \sin 2\phi$ (Fig. 2e,f), and $V^{2\omega}_{XY}$ in the HH measurement can be fit by $D^Y_{DL} \cos\phi + F^Y_{FL} \cos\phi \cos 2\phi$ (Fig. 2h).

For the intermediate values of ψ we find from ST-FMR measurements that the spin-torque efficiencies have the angular dependence shown in Fig. 3a–c. The behaviours of all three components are in excellent agreement with equations (1)–(3) for fitting parameters $C_0 = (26 \pm 4) \times 10^3\ (\Omega\,m)^{-1}$, $C_1 = (14 \pm 2) \times 10^3\ (\Omega\,m)^{-1}$ and $\theta_s = 44 \pm 5°$. This complete signature angular dependence, which corresponds to an **E**-induced spin current with tilted spin, has thus been verified experimentally in RuO_2. This is the most important result of this Article. It is a signature that the torques are indeed due to a spin current with a tilted spin orientation. Furthermore, the orientation of $\hat{s}$ is close to the optimum angle for maximizing the out-of-plane damping-like torque, 45° according to equation (3).

We can identify the ψ-dependent torques as being generated by the AF order in RuO_2 by comparing to measurements on (101)-oriented IrO_2 films, which are isostructural with RuO_2, but non-magnetic. The (101)-oriented IrO_2 films generate only conventional spin–orbit torques, with a non-zero value of $\xi^Y_{DL,E}$, but with $\xi^X_{DL,E} = 0$ and $\xi^Z_{DL,E} = 0$ (Fig. 4a). The lowered symmetry provided by the canted Néel vector of RuO_2 is therefore essential for the existence of the unconventional torque terms.

We mentioned above that the **E**-induced spin $\hat{s}$ is expected to be only approximately parallel to the Néel vector $\mathcal{N}$, as shown in

Fig. 1. This is not expected to be exact, because deviation from the Néel vector orientation can be generated by SOI. Assuming that $\mathcal{N}$ is oriented along the [001] direction of the RuO_2 crystal, and given the lattice constants of bulk RuO_2 (0.311 nm in the [001] direction and 0.449 nm in the [100] and [010] perpendicular directions), in a (101)-oriented film the tilt angle of $\mathcal{N}$ relative to the out-of-plane direction should be ~35°, a smaller tilt angle than for the spin orientation $\hat{s}$ indicated by the angular dependence in Fig. 3. This difference is qualitatively consistent with our density functional theory calculations, suggesting that for the AF-SHE, $\hat{s}$ is tilted from $\mathcal{N}$ for a (101)-oriented film by about 5° within the (010) plane due to SOI, which generates additional spin current components non-collinear to the Néel vector (Supplementary Section 4). Other possible contributions that might alter θ_s slightly are that $\mathcal{N}$ might not be oriented strictly along the [001] direction as reported in ref. [33], epitaxial strain can modify the lattice parameters slightly, and the interface spin transmission factor could depend on the orientation of the spin, so that spin absorbed by the ferromagnetic layer to generate the **E**-induced torque might not be exactly aligned with the spin orientation of the spin current within the RuO_2 layer. Related measurements of *E*-induced torque in (100)- and (110)-oriented RuO_2/ferromagnet bilayers, which are also consistent with a spin polarization approximately parallel to $\mathcal{N}$, have also recently been reported[44].

We measured the damping-like **E**-induced torques for different thicknesses of the (101)-oriented RuO_2 films (3–9 nm) as shown in Fig. 4b for measurements with $\psi=0°$ (filled squares) and $\psi=90°$ (open circles). Both the conventional (ψ-independent) and unconventional (ψ-dependent) torque efficiencies increase with increasing RuO_2 thickness, suggesting that the **E**-induced spin current originates in the bulk of the RuO_2 film rather than at the RuO_2/Py interface. The approach to saturation at larger thicknesses suggests a spin diffusion length[40] of 2.6 ± 0.3 nm in the RuO_2. Additional evidence for a bulk generation mechanism comes from samples in which we inserted a thin Ir spacer between the RuO_2 and the Py (the full structure was RuO_2(9 nm)/Ir(1 nm)/Py(4 nm)/Ir(1 nm)). In this case we still observe non-zero values of both $\xi^{y}_{DL,E} = (3.5 \pm 0.7) \times 10^4\ (\Omega\,m)^{-1}$ and $\xi^{z}_{DL,E} = (3.3 \pm 0.6) \times 10^3\ (\Omega\,m)^{-1}$ for $\psi=0°$ (Fig. 4c), only slightly reduced compared to RuO_2(9 nm)/Py(4 nm) with no spacer (Fig. 4b).

Based on the evidence we have presented so far, we have not determined whether the unconventional **E**-induced torques generated by RuO_2 correspond to a $\mathcal{T}$-odd or a $\mathcal{T}$-even spin current, because the AF order in RuO_2 allows both effects, and they could both generate spin currents with a well-defined orientation $\hat{s}$, giving a qualitatively similar dependence on the angle ψ (although, for the $\mathcal{T}$-even effect, $\hat{s}$ is not expected to be correlated to the Néel vector; Supplementary Section 4). Our measured SHCs are approximately a factor of 50 smaller than the prediction for the $\mathcal{T}$-odd spin current from a uniform single-domain RuO_2 sample (Fig. 1d and ref. [4]), but this could be due to nearly complete cancellation between domains with $\mathcal{N}$ in the [001] and [00$\bar{1}$] directions, structural disorder or a reduction in the electron relaxation time below the value assumed in the calculation. For the $\mathcal{T}$-odd mechanism to apply, as we noted above there must in fact be a small but consistent imbalance in the distribution of [001] and [00$\bar{1}$] domains, similar to the lack of complete cancellation between domains in other recent studies of spin torques from different antiferromagnets[20,21]. We also cannot rule out a contribution from the $\mathcal{T}$-even spin current based just on the amplitude of the torques, even though the predicted value is much smaller than the $\mathcal{T}$-odd spin current, because the predicted value of the $\mathcal{T}$-even torque is similar to the order of magnitude that we report here.

To help distinguish the $\mathcal{T}$-odd and $\mathcal{T}$-even mechanisms, we measured the out-of-plane damping-like SHC as a function of temperature (Fig. 4d). We observe a strong enhancement as a function of decreasing temperature. This is suggestive that the $\mathcal{T}$-odd spin current is dominant, as this should be enhanced as the electron lifetime increases at low temperature (Supplementary Section 4). Conventional $\mathcal{T}$-even SHCs arising from intrinsic SHEs generally have negligible temperature dependence for moderately low-resistivity materials like (101) RuO_2 (ref. [31]). We observe a non-zero out-of-plane damping-like torque up to at least 400 K (Fig. 4d), confirming that AF ordering in RuO_2 persists up to this temperature[32,33].

Even with the likelihood that the strength of the out-of-plane damping-like torque is reduced by cancellations between domain variants or other disorder, the strength of the effect is still among the largest of all materials that have been measured. For 6-nm-thick (101)-oriented RuO_2, from Fig. 3b we measure a maximum room-temperature value for the out-of-plane damping-like spin torque efficiency per unit electric field of $\xi^{z}_{DL,E} = (7 \pm 1) \times 10^3\ (\Omega\,m)^{-1}$ (compared to, for example, $(3.6 \pm 0.8) \times 10^3\ (\Omega\,m)^{-1}$ for WTe_2 (ref. [1]) and $(1.02 \pm 0.03) \times 10^3\ (\Omega m)^{-1}$ for $MoTe_2$ (ref. [45])). The only materials for which we are aware of a slightly larger out-of-plane damping-like spin-torque efficiency are the non-collinear antiferromagnet Mn_3GaN (ref. [20]) with $\xi^{z}_{DL,E} \approx 8.6 \times 10^3\ (\Omega\,m)^{-1}$ and (114)-textured $MnPd_3$ (ref. [22]) with $\xi^{z}_{DL,E} \approx 1.4 \times 10^4\ (\Omega\,m)^{-1}$. If our results are indeed due to a $\mathcal{T}$-odd spin current, the strength of the out-of-plane damping-like torque in RuO_2 might be increased substantially by controlling the AF domains to more strongly favour one of the domain variants ($\mathcal{N}$ parallel to [001] or [00$\bar{1}$]) over the other.

Conclusions

We have shown that (101)-oriented films of the collinear antiferromagnet RuO_2 can produce a substantial electric-field-generated out-of-plane damping-like torque on an adjacent permalloy film. The spin torques acting on the permalloy film were measured using ST-FMR and HH measurements. By analysing the dependence of the torques on the angles of both the electric field and the magnetic field relative to the crystal axes, we have shown that the torque is associated with a spin polarization approximately parallel to the Néel vector of the RuO_2. This angular dependence is the signature of an AF-SHE predicted for RuO_2 (ref. [23]).

Methods

Sample preparation. The RuO_2 thin films were prepared by reactive-oxide molecular beam epitaxy in a background pressure of 3×10^{-6} torr of distilled ozone (~80% O_3 + 20% O_2) at a substrate temperature of 310 °C. The films were then transported in air to a sputtering system with a base vacuum better than 2×10^{-8} torr, and 4 nm of Py was deposited at 30 mW power and 2 mtorr Ar pressure. To protect the Py layer from oxidation, we capped the Py with a 1.2 nm layer of Ta, which naturally oxidizes to TaO_x. Devices were then patterned by optical lithography and argon-ion milling such that electric current could be applied at different angles (ψ) with respect to the crystal axes. Electrical contacts for Ti(5 nm)/Pt(75 nm) were made by optical lithography, sputtering and liftoff. For the ST-FMR studies, the electrical contacts were in the form of a microwave-compatible ground–source–ground geometry (Fig. 1g), and the dimensions of the ST-FMR device under test were 30 μm × 20 μm (length × width). For the HH measurements the length and width of the Hall bars were 20 μm and 6 μm. Further details of sample preparation and characterization are provided in Supplementary Section 1.

HH measurements. For second-harmonic Hall measurements on (101)-oriented RuO_2/Py samples, the current axis of the Hall bar for different devices was aligned at various angles relative to the [010] crystal axis on the same sample chip ($\psi=0°$, 30°, 45°, 60°, 90°, 120°, 135° and 150°). We applied a low-frequency alternating current $I(t) = \Delta I \cos(2\pi f t)$ (with $f=1{,}327$ Hz) and an in-plane magnetic field H_{ext} at various angles ϕ relative to the current flow direction, and measured the first- and second-harmonic voltages using a lock-in amplifier. We investigated fixed values of $\mu_0 H_{ext}$ ranging from 50 to 300 mT, applied by a GMW projected-field magnet on a Newport motion-controlled stage. Further details of the measurements and analysis are provided in Supplementary Section 2.

ST-FMR measurements. For the ST-FMR measurements, we also patterned different devices on the same sample chip so that the applied microwave current had different angles, ψ, relative to the crystallographic axes, as shown in Supplementary Fig. 1a. For each device, an in-plane magnetic field was swept from

2,700 to 300 Oe at a variety of azimuthal angles, ϕ, with respect to the applied microwave current direction using a GMW projected-field magnet on a Newport motion-controlled stage. We applied microwave current amplitude-modulated at a reference frequency of 1,327 Hz using an Agilent current source and measured the ST-FMR mixing voltage using a lock-in amplifier. Further details about the analysis are provided in Supplementary Section 3.

Calculation of spin Hall conductivities. We calculate the atomic and electronic structures of RuO_2 using the projector augmented-wave (PAW) method[46] implemented in the VASP code[47]. A plane-wave cutoff energy of 500 eV and a $16\times16\times16$ **k**-point mesh in the irreducible Brillouin zone were used in the calculations. The exchange and correlation effects were treated within the generalized gradient approximation (GGA) developed by Perdew–Burke–Ernzerhof (PBE)[48]. The GGA+U functional[49,50] with $U_{\mathrm{eff}}=2$ eV on Ru 4*d* orbitals and $U_{\mathrm{eff}}=5$ eV on Ti 3*d* orbitals was included in all the calculations. The SOI was included in all the calculations. We used the tight-binding Hamiltonians obtained from the maximally localized Wannier functions[51] within the Wannier90 code[52]. The time-reversal odd and even parts of SHC are given by[15,53]

$$\sigma_{ij}^{k}=-\frac{e\hbar}{\pi}\int\frac{\mathrm{d}^3\mathbf{k}}{(2\pi)^3}\sum_{n,m}\frac{\Gamma^2\mathrm{Re}\left(\langle n\mathbf{k}|J_i^k|m\mathbf{k}\rangle\langle m\mathbf{k}|v_j|n\mathbf{k}\rangle\right)}{[(E_{\mathrm{F}}-E_{n\mathbf{k}})^2+\Gamma^2][(E_{\mathrm{F}}-E_{m\mathbf{k}})^2+\Gamma^2]},\tag{11}$$

and

$$\sigma_{ij}^{k}=-\frac{2e}{\hbar}\int\frac{d^3\mathbf{k}}{(2\pi)^3}\sum_{n'\neq n}\frac{\mathrm{Im}\left(\langle n\mathbf{k}|J_i^k|n'\mathbf{k}\rangle\langle n'\mathbf{k}|v_j|n\mathbf{k}\rangle\right)}{\left(E_{n\mathbf{k}}-E_{n'\mathbf{k}}\right)^2},\tag{12}$$

where $J_i^k=\frac{1}{2}\{v_i,s_k\}$ is the spin-current operator, $f_{n\mathbf{k}}$ is the Fermi-Dirac distribution function for band n and wavevector $\mathbf{k}$, v_i and s_k are velocity and spin operators, respectively, and $i,j,k=x,y,z$. A $500\times500\times500$ k-point mesh was used for the integral of equations (11) and (12). When calculating the $\mathcal{T}$-odd SHC in equation (11), a constant Γ that determines the broadening magnitude was used, which can be estimated by comparing the calculated conductivity with the experimental conductivity. For RuO_2 the room-temperature conductivities are 3,600 Ω^{-1} cm^{-1} for the (001) film and 6,900 Ω^{-1} cm^{-1} for the (101) film, corresponding to $\Gamma\approx50$ meV and $\Gamma\approx25$ meV, respectively. When calculating the $\mathcal{T}$-even SHC in equation (12), the adaptive smearing method[54] was used. Results of the calculations are presented in Supplementary Section 4.

Data availability

All the data accompanying this work are available at https://doi.org/10.5281/zenodo.6301100.

Received: 18 August 2021; Accepted: 11 March 2022;
Published online: 05 May 2022

References

1. MacNeill, D. et al. Control of spin–orbit torques through crystal symmetry in WTe_2/ferromagnet bilayers. *Nat. Phys.* **13**, 300–305 (2017).
2. MacNeill, D. et al. Thickness dependence of spin–orbit torques generated by WTe_2. *Phys. Rev. B* **96**, 054450 (2017).
3. Liu, L. et al. Symmetry-dependent field-free switching of perpendicular magnetization. *Nat. Nanotechnol.* **16**, 277–282 (2021).
4. DC, M. et al. Observation of anti-damping spin-orbit torques generated by in-plane and out-of-plane spin polarizations in $MnPd_3$. Preprint at https://arxiv.org/abs/2012.09315 (2020).
5. Taniguchi, T., Grollier, J. & Stiles, M. D. Spin-transfer torques generated by the anomalous Hall effect and anisotropic magnetoresistance. *Phys. Rev. Appl.* **3**, 044001 (2015).
6. Amin, V. P., Zemen, J. & Stiles, M. D. Interface-generated spin currents. *Phys. Rev. Lett.* **121**, 136805 (2018).
7. Amin, V. P., Li, J., Stiles, M. D. & Haney, P. M. Intrinsic spin currents in ferromagnets. *Phys. Rev. B* **99**, 220405 (2019).
8. Humphries, A. M. et al. Observation of spin–orbit effects with spin rotation symmetry. *Nat. Commun.* **8**, 911 (2017).
9. Baek, S. H. C. et al. Spin currents and spin–orbit torques in ferromagnetic trilayers. *Nat. Mater.* **17**, 509–513 (2018).
10. Bose, A. et al. Observation of anomalous spin torque generated by a ferromagnet. *Phys. Rev. Appl.* **9**, 064026 (2018).
11. Das, K. S., Liu, J., Van Wees, B. J. & Vera-Marun, I. J. Efficient injection and detection of out-of-plane spins via the anomalous spin Hall effect in permalloy nanowires. *Nano Lett.* **18**, 5633–5639 (2018).
12. Safranski, C., Montoya, E. A. & Krivorotov, I. N. Spin–orbit torque driven by a planar Hall current. *Nat. Nanotechnol.* **14**, 27–30 (2019).
13. Safranski, C., Sun, J. Z., Xu, J.-W. & Kent, A. D. Planar Hall driven torque in a ferromagnet/nonmagnet/ferromagnet system. *Phys. Rev. Lett.* **124**, 197204 (2020).
14. Ou, Y. et al. Exceptionally high, strongly temperature dependent, spin Hall conductivity of $SrRuO_3$. *Nano Lett.* **19**, 3663–3670 (2019).
15. Železný, J., Zhang, Y., Felser, C. & Yan, B. Spin-polarized current in noncollinear antiferromagnets. *Phys. Rev. Lett.* **119**, 187204 (2017).
16. Zhang, Y. et al. Strong anisotropic anomalous Hall effect and spin Hall effect in the chiral antiferromagnetic compounds Mn_3X (X = Sn, Ga, Ir, Rh, and Pt). *Phys. Rev. B* **95**, 075128 (2017).
17. Zhang, Y., Železný, J., Sun, Y., van den Brink, J. & Yan, B. Spin Hall effect emerging from a noncollinear magnetic lattice without spin–orbit coupling. *New J. Phys.* **20**, 073028 (2018).
18. Kimata, M. et al. Magnetic and magnetic inverse spin Hall effects in a non-collinear antiferromagnet. *Nature* **565**, 627–630 (2019).
19. Holanda, J. et al. Magnetic damping modulation in $IrMn_3/Ni_{80}Fe_{20}$ via the magnetic spin Hall effect. *Phys. Rev. Lett.* **124**, 087204 (2020).
20. Nan, T. et al. Controlling spin current polarization through non-collinear antiferromagnetism. *Nat. Commun.* **11**, 4671 (2020).
21. Chen, X. et al. Observation of the antiferromagnetic spin Hall effect. *Nat. Mater.* **20**, 800–804 (2021).
22. Hu, S. et al. Efficient field-free perpendicular magnetization switching by a magnetic spin Hall effect. Preprint at https://arxiv.org/abs/2103.09011 (2021).
23. González-Hernández, R. et al. Efficient electrical spin splitter based on nonrelativistic collinear antiferromagnetism. *Phys. Rev. Lett.* **126**, 127701 (2021).
24. Šmejkal, L., Sinova, J. & Jungwirth, T. Altermagnetism: spin-momentum locked phase protected by non-relativistic symmetries. Preprint at https://arxiv.org/abs/2105.05820 (2021).
25. Hayami, S., Yanagi, Y. & Kusunose, H. Momentum-dependent spin splitting by collinear antiferromagnetic ordering. *J. Phys. Soc. Jpn* **88**, 123702 (2019).
26. Yuan, L.-D., Wang, Z., Luo, J.-W., Rashba, E. I. & Zunger, A. Giant momentum-dependent spin splitting in centrosymmetric low-*Z* antiferromagnets. *Phys. Rev. B* **102**, 014422 (2020).
27. Bose, A. et al. Effects of anisotropic strain on spin–orbit torque produced by the Dirac nodal line semimetal IrO_2. *ACS Appl. Mater. Interfaces* **12**, 55411–55416 (2020).
28. Sun, Y., Zhang, Y., Liu, C.-X., Felser, C. & Yan, B. Dirac nodal lines and induced spin Hall effect in metallic rutile oxides. *Phys. Rev. B* **95**, 235104 (2017).
29. Jadaun, P., Register, L. F. & Banerjee, S. K. Rational design principles for giant spin Hall effect in 5*d*-transition metal oxides. *Proc. Natl Acad. Sci. USA* **117**, 11878 (2020).
30. Uchida, M., Nomoto, T., Musashi, M., Arita, R. & Kawasaki, M. Superconductivity in uniquely strained RuO_2 films. *Phys. Rev. Lett.* **125**, 147001 (2020).
31. Ruf, J. P. et al. Strain-stabilized superconductivity. *Nat. Commun.* **12**, 59 (2021).
32. Berlijn, T. et al. Itinerant antiferromagnetism in RuO_2. *Phys. Rev. Lett.* **118**, 077201 (2017).
33. Zhu, Z. H. et al. Anomalous antiferromagnetism in metallic RuO_2 determined by resonant X-ray scattering. *Phys. Rev. Lett.* **122**, 017202 (2019).
34. Feng, Z. et al. Observation of the anomalous Hall effect in a collinear antiferromagnet. Preprint at https://arxiv.org/abs/2002.08712 (2020).
35. Šmejkal, L., González-Hernández, R., Jungwirth, T. & Sinova, J. Crystal time-reversal symmetry breaking and spontaneous Hall effect in collinear antiferromagnets. *Sci. Adv.* **6**, eaaz8809 (2020).
36. Shao, D.-F., Zhang, S.-H., Li, M., Eom, C.-B. & Tsymbal, E. Y. Spin-neutral currents for spintronics. *Nat. Commun.* **12**, 7061 (2021).
37. Šmejkal, L., Hellenes, A. B., González-Hernández, R., Sinova, J. & Jungwirth, T. Giant and tunneling magnetoresistance in unconventional collinear antiferromagnets with nonrelativistic spin-momentum coupling. *Phys. Rev. X* **12**, 011028 (2022).
38. Mook, A., Neumann, R. R., Johansson, A., Henk, J. & Mertig, I. Origin of the magnetic spin Hall effect: spin current vorticity in the Fermi sea. *Phys. Rev. Res* **2**, 023065 (2020).
39. Karimeddiny, S., Mittelstaedt, J. A., Buhrman, R. A. & Ralph, D. C. Transverse and longitudinal spin-torque ferromagnetic resonance for improved measurement of spin–orbit torque. *Phys. Rev. Appl.* **14**, 024024 (2020).
40. Liu, L., Moriyama, T., Ralph, D. C. & Buhrman, R. A. Spin-torque ferromagnetic resonance induced by the spin Hall effect. *Phys. Rev. Lett.* **106**, 036601 (2011).
41. Fang, D. et al. Spin–orbit-driven ferromagnetic resonance. *Nat. Nanotechnol.* **6**, 413–417 (2011).
42. Hayashi, M., Kim, J., Yamanouchi, M. & Ohno, H. Quantitative characterization of the spin–orbit torque using harmonic Hall voltage measurements. *Phys. Rev. B* **89**, 144425 (2014).
43. Avci, C. O. et al. Interplay of spin–orbit torque and thermoelectric effects in ferromagnet/normal-metal bilayers. *Phys. Rev. B* **90**, 224427 (2014).
44. Bai, H. et al. Observation of spin splitting torque in a collinear antiferromagnet RuO_2. Preprint at https://arxiv.org/abs/2109.05933 (2021).
45. Stiehl, G. M. et al. Layer-dependent spin-orbit torques generated by the centrosymmetric transition metal dichalcogenide β-$MoTe_2$. *Phys. Rev. B* **100**, 184402 (2019).

46. Kresse, G. & Joubert, D. From ultrasoft pseudopotentials to the projector augmented-wave method. *Phys. Rev. B* **59**, 1758–1775 (1999).
47. Kresse, G. & Furthmüller, J. Efficient iterative schemes for ab initio total-energy calculations using a plane-wave basis set. *Phys. Rev. B* **54**, 11169–11186 (1996).
48. Perdew, J. P., Burke, K. & Ernzerhof, M. Generalized gradient approximation made simple. *Phys. Rev. Lett.* **77**, 3865–3868 (1996).
49. Anisimov, V. I., Zaanen, J. & Andersen, O. K. Band theory and Mott insulators: Hubbard U instead of Stoner I. *Phys. Rev. B* **44**, 943–954 (1991).
50. Dudarev, S. L., Botton, G. A., Savrasov, S. Y., Humphreys, C. J. & Sutton, A. P. Electron-energy-loss spectra and the structural stability of nickel oxide: an LSDA+U study. *Phys. Rev. B* **57**, 1505–1509 (1998).
51. Marzari, N., Mostofi, A. A., Yates, J. R., Souza, I. & Vanderbilt, D. Maximally localized Wannier functions: theory and applications. *Rev. Mod. Phys.* **84**, 1419–1475 (2012).
52. Mostofi, A. A. et al. An updated version of wannier90: a tool for obtaining maximally-localised Wannier functions. *Comput. Phys. Commun.* **185**, 2309–2310 (2014).
53. Sinova, J., Valenzuela, S. O., Wunderlich, J., Back, C. H. & Jungwirth, T. Spin Hall effects. *Rev. Mod. Phys.* **87**, 1213–1260 (2015).
54. Yates, J. R., Wang, X., Vanderbilt, D. & Souza, I. Spectral and Fermi surface properties from Wannier interpolation. *Phys. Rev. B* **75**, 195121 (2007).

Acknowledgements

We thank T. M. Cham for discussions. This research was supported by the US Department of Energy, DE-SC0017671 (R.J. and partial support for A.B.), the National Science Foundation (NSF) MRSEC programme through the Cornell Center for Materials Research, DMR-1719875 (X.S.Z. and partial support for A.B.), the NSF Platform for the Accelerated Realization, Analysis and Discovery of Interface Materials (PARADIM) under cooperative agreement no. 2039380 (N.J.S., H.P.N., J.S. and D.G.S.), the Gordon and Betty Moore Foundation's EPiQS Initiative, grant GBMF9073 (D.G.S.), the NSF MRSEC programme, DMR-1420645 (D.-F.S.), and the NSF MRI programme, DMR-1429155 (X.Z.). The devices were fabricated using the shared facilities of the Cornell NanoScale Facility, a member of the National Nanotechnology Coordinated Infrastructure (supported by the NSF, NNCI-2025233) and the facilities of Cornell Center for Materials Research.

Author contributions

A.B. played the primary role in sample fabrication and, together with R.J., led the spin-torque measurements and data analysis, supervised by D.C.R. N.J.S., H.P.N. and J.S. grew the RuO_2 and IrO_2 films, supervised by D.G.S. D.-F.S. performed the DFT calculations, supervised by E.Y.T. X.S.Z. performed STEM imaging, supervised by D.A.M. A.B., R.J. and D.C.R. led the writing of the manuscript, with participation by all of the authors.

Competing interests

The authors declare no competing interests.

Additional information

Supplementary information The online version contains supplementary material available at https://doi.org/10.1038/s41928-022-00744-8.

Correspondence and requests for materials should be addressed to Daniel C. Ralph.

Peer review information *Nature Electronics* thanks Feng Pan and the other, anonymous, reviewer(s) for their contribution to the peer review of this work.

Reprints and permissions information is available at www.nature.com/reprints.

Publisher's note Springer Nature remains neutral with regard to jurisdictional claims in published maps and institutional affiliations.